Biomedicine & Pharmacotherapy 173 (2024) 116380

Contents lists available at ScienceDirect

Biomedicine & Pharmacotherapy

journal homepage: www.elsevier.com/locate/biopha

FM19G11-loaded nanoparticles modulate energetic status and production of reactive oxygen species in myoblasts from ALS mice

Claudia Malacarne [a], Eleonora Giagnorio [a,*], Cristina Chirizzi [b,c], Marco Cattaneo [d,e], Fulvia Saraceno [a,f], Paola Cavalcante [a], Silvia Bonanno [a], Renato Mantegazza [a], Victoria Moreno-Manzano [g], Giuseppe Lauria [d,h], Pierangelo Metrangolo [c,i], Francesca Baldelli Bombelli [c], Stefania Marcuzzo [a,i,**]

[a] Neuroimmunology and Neuromuscular Diseases Unit, Fondazione IRCCS Istituto Neurologico Carlo Besta, Via Celoria 11, Milan 20133, Italy
[b] Neuroradiology Unit, Fondazione IRCCS Istituto Neurologico Carlo Besta, Via Celoria 11, Milan 20133, Italy
[c] Laboratory of Supramolecular and Bio-Nanomaterials (SupraBioNano Lab), Department of Chemistry, Materials and Chemical Engineering, "Giulio Natta", Politecnico di Milano, Milan 20131, Italy
[d] Neuroalgology Unit, Fondazione IRCCS Istituto Neurologico Carlo Besta, Via Celoria 11, Milan 20133, Italy
[e] PhD Program in Pharmacological Biomolecular Sciences, Experimental and Clinical, University of Milano, Via G.Balzaretti 9, Milan 20133, Italy
[f] Department of Chemistry, Life Sciences and Environmental Sustainability, University of Parma, Parco Area delle Scienze 11/a, Parma 43124, Italy
[g] Neuronal and Tissue Regeneration Laboratory, Prince Felipe Research Center, Carrer dÆduardo Primo Yúfera 3, Valencia 46012, Spain
[h] Department of Medical Biotechnology and Translational Medicine, University of Milano, Milan 20133, Italy
[i] Brains Lab, Joint Research Platform, Fondazione IRCCS Istituto Neurologico Carlo Besta-Politecnico di Milano, Via Celoria 11, 20133 Milan, Italy

ARTICLE INFO

Keywords:
Amyotrophic lateral sclerosis
Muscle
FM19G11
G93A-SOD1 mouse model
Nanomedicine

ABSTRACT

Amyotrophic lateral sclerosis (ALS) is a progressive neurodegenerative disease affecting motor neurons. Considerable evidence indicates that early skeletal muscle atrophy plays a crucial role in the disease pathogenesis, leading to an altered muscle-motor neuron crosstalk that, in turn, may contribute to motor neuron degeneration. Currently, there is no effective treatment for ALS, highlighting the need to dig deeper into the pathological mechanisms for developing innovative therapeutic strategies. FM19G11 is a novel drug able to modulate the global cellular metabolism, but its effects on ALS skeletal muscle atrophy and mitochondrial metabolism have never been evaluated, yet.

This study investigated whether FM19G11-loaded nanoparticles (NPs) may affect the bioenergetic status in myoblasts isolated from G93A-SOD1 mice at different disease stages. We found that FM19G1-loaded NP treatment was able to increase transcriptional levels of Akt1, Akt3, Mef2a, Mef2c and Ucp2, which are key genes associated with cell proliferation (Akt1, Akt3), muscle differentiation (Mef2c), and mitochondrial activity (Ucp2), in G93A-SOD1 myoblasts. These cells also showed a significant reduction of mitochondrial area and networks, in addition to decreased ROS production after treatment with FM19G11-loaded NPs, suggesting a ROS clearance upon the amelioration of mitochondrial dynamics.

Our overall findings demonstrate a significant impact of FM19G11-loaded NPs on muscle cell function and bioenergetic status in G93A-SOD1 myoblasts, thus promising to open new avenues towards possible adoption of FM19G11-based nanotherapies to slow muscle degeneration in the frame of ALS and muscle disorders.

1. Introduction

Amyotrophic lateral sclerosis (ALS) is a neurodegenerative disease characterized by upper and lower motor neuron loss associated with muscle atrophy, paralysis, and eventually death. The majority of cases is sporadic (sALS) with no family history, whereas 10% presents a gene mutation that runs in the family (fALS). In 20% of patients, the mutation is linked to the superoxide dismutase 1 (SOD1) gene [1]. Currently,

* Corresponding author.
** Corresponding author at: Neuroimmunology and Neuromuscular Diseases Unit, Fondazione IRCCS Istituto Neurologico Carlo Besta, Via Celoria 11, Milan 20133, Italy.
E-mail addresses: eleonora.giagnorio@istituto-besta.it (E. Giagnorio), stefania.marcuzzo@istituto-besta.it (S. Marcuzzo).

https://doi.org/10.1016/j.biopha.2024.116380
Received 27 November 2023; Received in revised form 22 February 2024; Accepted 29 February 2024
Available online 5 March 2024

there is no effective treatment for the disease [2], highlighting the need to dig deeper into the pathological mechanisms for the development of novel therapeutic strategies. On this point, the G93A-SOD1 transgenic mouse has been the most extensively used animal model to investigate key features of ALS pathology and develop preclinical therapies [3].

ALS is a multisystem disorder and evidence indicates early damages in the motor neuron-muscle crosstalk, suggesting that skeletal muscle alterations could play a crucial role in the disease pathogenesis [4,5]. Indeed, muscle-restricted expression of mutant SOD1 is sufficient to induce neuromuscular junction (NMJ) alterations and may lead to motor neuron death [6]. A variety of mechanisms have been proposed to underpin the muscle-related ALS pathology, including excitotoxicity, mitochondrial dysfunction, and oxidative stress [7]. Defects in cellular bioenergetics linked to mitochondrial structure, and function have been observed in the skeletal muscle of both sALS and fALS patients [8]. Similarly, in the G93A-SOD1 mice accumulation of SOD1 aggregates in mitochondrial intermembrane space and matrix have been found to cause abnormal mitochondrial network and reduce mitochondrial dynamics, resulting in intrinsic muscle damage early before motor neuron axonal withdrawal [9,10]. A disease-stage-dependent reduction in autophagy capacity, likely leading to the accumulation of damaged mitochondria, was observed in the ALS mouse muscle [11]. It is known that mitochondria provide cellular energy in the form of ATP *via* oxidative phosphorylation, but they generate reactive oxygen species (ROS) during oxidative metabolism. Altered mitochondria are the major source of excessive ROS production, producing approximately 90% of cellular ROS [12] which, in turn, further aggravate mitochondrial alterations promoting muscle wasting in G93A-SOD1 mice [13]. Mammalian cells have evolved to handle such a stress via various endogenous anti-oxidant proteins. These proteins include the family of mitochondrial uncoupling proteins (UCPs), which are anionic carriers located in the mitochondrial inner membrane. Wheras the UCP1 homolog plays an important role in adaptive thermogenesis in brown adipose tissue [14], the highly homologous UCP2 and UCP3, have been described to prevent the formation of reactive oxygen species [15]. A long-term uncoupling of mitochondria and prolonged ATP reduction are detrimental for the cells [16]. Indeed, valosin-containing protein (VCP) mutations occurring in 1–2% of fALS cause profound mitochondrial uncoupling resulting in a significant reduction of cellular ATP production, making cells more vulnerable to degenerative processes [17]. However, a transient or mild mitochondrial uncoupling, leading to the reduction of oxidative stress and superoxide production [18], could result in neuroprotection [19], thus suggesting a role for UCPs as possible targets for therapeutic interventions in ALS [20].

The FM19G11 compound was identified as an inhibitor of the hypoxia inducible factor 1 α (HIF1α) under hypoxic conditions, resulting in an increase of neural precursor cells (NPCs) differentiation in rats after spinal cord injury with the modulation of SRY-related HMG-box 2 (Sox2) and octamer-binding transcription factor 4 (Oct4) gene expression [21]. Later, Rodriguez-Jimenez and colleagues demonstrated that under normoxia in the absence of HIF1α, the drug is able to activate the global cellular metabolism of NPCs by inducing mitochondrial uncoupling process, which leads to a transient reduction of ATP levels. Of note, this phenomenon was found to trigger an adaptive cellular response, generating a compensatory increase of the glucose uptake *via* the activation of AMP-activated protein kinase (AMPK) and protein kinase B (AKT) signaling pathways to provide energy through ATP synthesis. Moreover, after 24 h of FM19G11 treatment, a positive evolution of mitochondrial activity in terms of increased expression of mitochondrial genes and biosynthesis was demonstrated in stem cells derived from spinal cord injured rats [22]. In the ALS landscape, our previous study demonstrated a positive effect of FM19G11 on self-renewal and proliferation of NPCs derived from G93A-SOD1 mice by the activation of genes associated with pluripotency, self-renewal, proliferation, and mitochondrial uncoupling process, hence providing preliminary but promising evidence for the development of a novel approach to counteract motor neuron degeneration [23]. However, the effect of FM19G11 on ALS skeletal muscle atrophy and mitochondrial metabolism has never been evaluated yet.

In the present study we investigated the effect of FM19G11 treatment on cellular bioenergetics in myoblasts isolated from G93A-SOD1 mice during disease progression using a nanoparticle (NP)-based drug delivery system (DDS). Indeed, FM19G11 is poorly soluble in the aqueous environment hence, to improve its bioavailability, controlled release and cellular uptake, we developed a DDS composed of NP made of the FDA-approved poly (lactic-co-glycolic acid) (PLGA), which is among the most attractive polymeric materials for biomedical applications, thanks to its high biocompatibility and biodegradability, long-term storage stability, and ability to encapsulate and protect drugs from fast degradation *in vivo*.

By molecular analyses and functional studies, we assessed cellular proliferation and differentiation, as well as mitochondrial network dynamics and ROS production, in the treated myoblasts. We observed an increase of the energetic status and a reduction of the mitochondrial network area in G93A-SOD1 myoblasts under FM19G11-loaded NP treatment. Of interest, the treatment was able to reduce the ROS production in myoblasts derived from animals at the symptomatic disease stage.

Our overall findings could represent a key step towards a better understanding of the skeletal muscle-related ALS pathogenesis, and provide a proof-of-concept case for the development of muscle-targeting therapeutic strategies to be translated into ALS clinical practice.

2. Material and methods

2.1. Animal model

All animal experiments were carried out in accordance with the EU Directive 2010/63 and with the Italian law (D.L. 26/2014) on the protection of animals used for scientific purposes. Transgenic G93A-SOD1 (B6SJL-Tg (SOD1*G93A)1Gur/J) [MGI: 2183719] and control B6.SJL mice were purchased from Charles River Laboratories, Inc. (Wilmington, MA, USA), maintained and bred at the animal house of the Fondazione IRCCS Istituto Neurologico Carlo Besta in compliance with institutional guidelines. The project was approved by the Ethics Committee of the Institute and the Italian Ministry of Health (ref. 78/2022-PR). Transgenic G93A-SOD1 progenies were identified by quantitative real-time PCR amplification of the mutant human SOD1 gene, as previously described [4]. G93A-SOD1 male animals carrying more than 27 mutant SOD1 copies were included in the study. Mice were sacrificed for tissue collection by CO_2 exposure at week 8 (pre-symptomatic stage of the disease), 12 (disease onset), and 18 (end stage of the disease).

2.2. Nanoparticle synthesis and drug loading

The NPs were prepared by the solvent evaporation method using polyvinyl alcohol (PVA; 30–70 kDa, 87–90% hydrolyzed; Sigma-Aldrich, Germany) as surfactant to provide the required colloidal stability in the biological environment reducing protein adsorption on NP surface [24]. Briefly, FM19G11 (Sigma-Aldrich, Germany) was solubilized in dichloromethane (DCM) to prepare a solution at 0.5 mg mL^{-1} concentration. Then, 20 mg of polymer (PLGA; Resomer 502 H, 50:50, 7–17 kDa; Sigma-Aldrich, Germany) were solubilized in 1 mL of the FM19G11 solution. The resulting organic phase was drop-wise added to 4 mL of aqueous solution, containing 2% w/v PVA. The solution was then sonicated using a tip sonicator at 60 W for 60 s (two sonication cycles, each lasting 30 seconds, with a 30-second break between them). Samples were left stirring for 3 h and the excess of organic solvent was removed by rotavapor. NPs were collected and purified by centrifugation (10 733 g × 40 min). The final product was resuspended in 1 mL of MilliQ water (mQw) and the unloaded drug was removed through a mild centrifugation (10 733 g × 1 min). Fluorescently labeled NPs were

obtained in the same way, by also adding 2% w/w of rhodamine B-labeled PLGA (50:50, 10–30 kDa; Sigma-Aldrich, Germany) to the final PLGA solution in the organic phase.

NPs were characterized through dynamic light scattering (DLS) analysis in order to estimate their hydrodynamic diameter (D_H). Measurements were performed on an ALV apparatus equipped with ALV-5000/EPP Correlator, special optical fiber detector and ALV/CGS-3 Compact goniometer. The light source is He–Ne laser (l = 633 nm), 22 mW output power. Hydrodynamic size and related distribution were determined by a cumulant fitting of the auto-correlation function. For these analyses, the stock NP dispersion was diluted 1:100 (v/v) in water and measured at 25 °C. In the specific case of FM19G11-loaded NPs, obtained size distribution showed an averaged hydrodynamic diameter ($<D_H>$) of 227 ± 7 nm.

FM19G11 content was determined by HPLC analysis. The NPs were disassembled by mixing the NP suspension with dimethyl sulfoxide (DMSO) at a volume ratio of 1/10. Each sample was injected (20 μL) in a C18 reversed-phase chromatography column at 30 °C with a flow rate of 0.5 mL min^{-1} in a solution of acetonitrile-water with 59:41 ratio. The FM19G11 peak was detected after ~7 min. The detection wavelength was set at 247 nm. Calibration curves were previously obtained with different FM19G11 concentrations (0.25, 0.1, 0.04, 0.02, 0.01, 0.004, 0.002 mg mL^{-1}). Encapsulation Efficiency (EE%) values associated to each batch of NPs were calculated according to the following equations: EE% = 100*(Weight of Drug Encapsulated in Polymer Nanoparticles)/(Weight of Drug Used in Encapsulation Method). The obtained value of EE% was 51.5 ± 9.8% corresponding to 0.56 ± 0.02 mM of FM19G11.

The analyses were performed on a JASCO® HPLC equipped with: 2057 autosampler; RI-2031 refraction index detector; UV-/Vis detector, CO-2060 plus oven column; PU-2080 pump; MD-2018 photodiode array PDA detector; C18 column (2.7 mm particle size) 150 mm×4.6 mm (length x diameter). Evaluation of the drug concentration was done using the UV-/Vis detector.

2.3. Primary myoblast culture and FM19G11 treatment

Gastrocnemius muscles were obtained from G93A-SOD1 and control mice. After euthanizing mice by CO_2 inhalation, skin was removed from the hind-limbs to expose muscles. Then, with sterilized scissors and forceps, gastrocnemius muscles from both hind-limbs were collected and placed into one well of 6-well plate containing 1 × Dulbecco's phosphate-buffered saline (D-PBS) (Thermo Fisher Scientific, Waltham, Massachusetts, USA) and 1% penicillin and streptomycin (Pen/Strep) on ice. In a sterile tissue culture hood, mince the muscles in 1–2 mm pieces with razor blades and place them in a 25 cm^2 culture flask (Corning, New York, USA). Let them dry for about 10 min then 5 mL of proliferation culture medium was added to each flask and incubated at 37°C with 5% CO2 for about 10 days, with no medium change. Proliferation medium consisted of DMEM (Thermo Fisher Scientific) supplemented with 20% FBS (Thermo Fisher Scientific), 1% Pen/Strep, 1% Glutamine (Euroclone, Milan, Italy), 1% Insulin (Sigma-Aldrich, St. Louis, Missouri, USA), 10 ng/mL EGF, and 10 ng/mL FGF (Thermo Fisher Scientific). After approximately 10 days from dissociation, myoblasts appeared from the muscle biopsy. For subsequent subcultures, myoblasts at 70–90% confluency were rinsed with D-PBS (Thermo Fisher Scientific), then collected with a Trypsin/EDTA solution (Euroclone), incubated at 37°C with 5% CO_2 for 5–10 min, and centrifuged at 1200 rpm for 10 min at RT (cell passage 1, P1). This was repeated until day 25 (P3) of in vitro cultures in order to obtain sufficient cells for further analyses. At P3, the G93A-SOD1 and control myoblasts were seeded in proliferative medium at a density of 6 ×10^4 cells at different growth conditions: i) basal condition (i.e. untreated cells); ii) FM19G11 (Sigma)-loaded NPs (corresponding to 500 nM of FM19G11 and NPs); iii) FM19G11 (Sigma)-loaded NPs (1 μM of FM19G11 and NPs). Cells were maintained in culture for 48 and 72 h, and further collected for immunofluorescence and molecular analysis. By Trypan blue exclusion method, the number of viable cells was assessed in untreated and treated myoblasts isolated from of 8-week-old control and G93A-SOD1 mice, from passage 3.

2.4. Quantitative real-time PCR

Total RNA was extracted from cells (5–8 ×10^5) using Trizol reagent (Thermo Fisher Scientific) and quantified using 2100 Nano Bioanalyzer (Agilent Technologies, Santa Clara, California, USA). Next, RNA samples were reverse transcribed to cDNA using the SuperScript™ VILO™ cDNA Synthesis Kit (Thermo Fisher Scientific). cDNA was amplified in duplicate by quantitative real-time PCR using TaqMan™ Fast Advanced Master Mix and TaqMan Array Fast Plate assembled by Thermo Fisher Scientific with primer and probes for AKT serine/threonine kinase (Akt) 1 (Assay ID: Mm01331626_m1), Akt3 (Assay ID: Mm00442194_m1), Myocyte-specific enhancer factor (Mef) 2a (Assay ID: Mm01318991_m1), Mef2c (Assay ID: Mm01340842_m1), glucose transporter (Glut) 4 (ID: Mm00436615_m1), Uncoupling Protein (Ucp) 2 (ID: Mm00627599_m1), and the 18 S housekeeping (Corrisponding Assay ID: Hs99999901_s1) genes on ViiA7 Real-time PCR system (Thermo Fisher Scientific). mRNA expression levels were normalized against 18 S, and the relative values were calculated using the $2^{-\Delta Ct}$ × 1000 formula.

2.5. Immunofluorescence

Before the fixation, the cells were washed with PBS for three times and then were fixed using 4% paraformaldehyde (Sigma) in PBS pH 7.4 for 15 min at room temperature (RT). Permeabilization and blocking were performed using 0.25% Triton X-100 (Carlo Erba Reagents, Milan, Italy) and 10% Normal Goat Serum (Thermo Fisher Scientific) in PBS for 1 h at RT. Next, cells were incubated over night at 4°C with the rabbit anti-desmin antibody (1:50; Thermo Fisher Scientific). Immunopositivity was revealed with Alexa Fluor 488-conjugated goat ant-rabbit IgG (1:500; Thermo Fisher Scientific). Cell nuclei were stained with 1 μg/mL 4′, 6-diamidino-2-phenylindole (DAPI; 1:1000; Thermo Fisher Scientific). Images were acquired using a confocal microscope (Eclipse TE-2000-E, Nikon, Tokyo, Japan) and the number of internalized nanoparticles in cells was calculated with the Fiji-ImageJ software (version 2.3.0/1.53q).

2.6. Analysis of mitochondrial network morphology

To analyze the morphology of the mitochondrial network, coverslip adherent-myoblasts were first treated with non-fluorescent FM19G11-loaded NPs for 72 h. After 72 h cells were incubated for 30 min at 37°C and 5% CO_2 with a solution of 200 nM MitoTracker® Orange CMTMRos (Thermo Fisher Scientific). Cells were then fixed using 4% paraformaldehyde (Sigma) in PBS pH 7.4 for 15 min at RT, permeabilized and blocked via 0.25% Triton X-100 and 10% Normal Goat Serum in PBS for 1 h at RT and incubated with 1 μg/mL DAPI for 10 min to stain cell nuclei. Finally, cells were observed under the confocal microscope (Eclipse TE-2000-E, Nikon) and analyzed using the Image J software (version 2.3.0/1.53q). Morphological analysis of active mitochondria was performed using the MiNA (Mitochondrial Network Analysis) 2.0 plug-in of ImageJ, available at https://github.com/StuartLab [25]. MiNA provides simplified image analysis methods to evaluate the mitochondrial branching and networks. In particular, it performs a semi-automated analysis by first generating a sharp, high contrast image, exhibiting minimal noise; secondly, the image is converted in a binary image and thirdly in a skeleton image, which is used for the quantitative analysis. MiNA plugin classifies each pixel of a skeleton image and, according to how the pixels are spatially related one to each other, mitochondria are classified as 1) individuals, characterized by rod, punctate or large/round morphology; 2) networks, which are a large continuous reticulum of multiple mitochondria. Each network contains at least one junction and more than one branch. MiNA

specifically computes the number of individuals, which is the number of objects that does not contain a junction pixel, and corresponds to the number of mitochondria that are not part of a network. Regarding the network analysis, MiNA accurately provides the: 1) number of networks, corresponding to the number of objects that contains at least one junction pixel; the number of networks is indicative of the balance between the fission and fusion processes, where the mitochondria divides into one or more independent structure (individuals), or are fused resulting in thin and elongated highly interconnected mitochondrial network; 2) mean length of network branches; 3) median length of network branches; 4) standard deviation of network branch lengths; 5) mean number of branches per network; 6) median number of branches per network; and 7) standard deviation of the number of branches per network. These parameters quantify the extension of the mitochondrial networks and how statistically disperse they are. Finally, MiNA enables the mitochondrial footprint analysis, which calculates the total area or volume of the image consumed by the lengths of mitochondrial structure using a topological skeleton [25]. The generated images were analyzed as previously described by Iannetti *et al.* [26]. Briefly, the images were opened on ImageJ and processed as follows: 1-Process/Filters/UnsharpMask; 2-Process/EnhanceLocal Contrast (CLAHE); 3-Process/Filters/-Median; 4-Process/Binary/MakeBinary; 5-Process/Binary/Skeletonize; 6-Analyze/Skeleton/AnalyzeSkeleton(2D/3D); 7 Plugins/StuartLab/MiNAScripts/MiNAAnalyzeMorphology, with Tophat mask strength preprocessing.

2.7. ROS detection

To quantify and investigate the ROS production after 72 h of treatment with FM19G11-loaded NPs, coverslip adherent-myoblasts were incubated with a solution of 5 μM CellROX Green Reagents (Thermo Fisher Scientific) and 1 μg/mL DAPI to stain cell nuclei for 30 min at 37°C and 5% CO_2. As positive control, the same cells were treated with 0.5 mM H_2O_2 for 1 h. Next, the medium was removed and three washes with D-PBS were performed. Finally, cells were fixed with 4% paraformaldehyde for 15 min at RT and the fluorescent signal was analyzed within 24 h using the confocal microscope (Nikon) and the Image J software (version 2.3.0/1.53q). Fluorescence intensity of each cell was calculated as previously described by McCloy et al. [27]. For each image, three background areas were used to normalize autofluorescence values.

2.8. Statistical analysis

The non-Gaussian distributed data, verified via Shapiro–Wilk test, were analyzed either with Mann–Whitney test for the comparison of two groups or Kruskall-Wallis test followed by Dunn analysis for multiple group comparisons. p-values < 0.05 were considered statistically significant. GraphPad Prism version 5.0 for Windows (GraphPad Software; San Diego, California, USA) was used for data elaboration and statistical analysis.

3. Results

3.1. Development of optimal myoblast treatment with FM19G11-loaded NPs

To determine the optimal FM19G11-loaded treatment condition, we cultured G93A-SOD1 myoblasts derived from 18-week-old mice under the following growth conditions for 48 and 72 h: i) untreated cells; ii) FM19G11-loaded NP treatment (500 nM of FM19G11 and NPs); iii) FM19G11-loaded NP treatment (1 μM of FM19G11 and NPs). As shown in Fig. 1A, NPs are internalized and maintained at least for 72 h in the cytoplasm. Importantly, a better cellular growth rate was observed using the 500 nM than the 1uM concentration. Based on these findings, we established that the optimal condition for myoblast treatment with FM19G11-loaded NPs was using a FM19G11 concentration of 500 nM and an incubation time of 72 h. Of note, NPs localized in the cytoplasm of the treated myoblasts (Fig. 1C) and no significant differences in NP internalization between the G93A-SOD1 and control cells were observed (Fig. 1D). We assessed the number of viable cells using the Trypan blue exclusion method in treated and untreated myoblast cultures. A significant increase of the number of viable cells was observed in FM19G11-loaded NP treated cells from 8-week-old control and G93A-SOD1 mice compared to the untreated cells (Supplemental Fig. 1, $p < 0.01$).

3.2. Increased Akt1 and Akt3 expression in G93A-SOD1 myoblasts treated with FM19G11-loaded NPs

Upon 72 h of treatment, our molecular analysis demonstrated a significant upregulation of the expression levels of Akt1, a gene involved in myogenesis [28], in FM19G11-loaded NP-treated G93A-SOD1 myoblasts compared to G93A-SOD1 untreated (Fig. 2A, $p < 0.05$) and treated control cells isolated at the presymptomatic stage of disease (8 weeks), but not in untreated G93A-SOD1 cells compared to untreated control cells and in untreated compared to treated control cells.

Moreover, increased mRNA levels of Akt3, another myogenesis-related gene, were observed in treated 12-week G93A-SOD1 mouse myoblasts compared to treated myoblasts from 12-week control animals (Fig. 2B, $p < 0.01$), but not in untreated G93A-SOD1 cells compared to untreated control cells and in untreated compared to treated control cells. These data suggested that the FM19G11 treatment with NPs is able to trigger a proliferative response in G93A-SOD1, but not in control, myoblasts at early disease stages as an attempt to counteract the Akt-related molecular defects arising in the muscle cells, though the Akt1 and Akt3 expression levels are not altered in untreated cells of diseased compared to control animals.

3.3. Increased Mef2a and Mef2c expression in G93A-SOD1 myoblasts treated with FM19G11-loaded NPs

To dig deeper into the molecular events underlying muscle cell development upon FM19G11-loaded NP treatment, we analyzed the expression levels of Mef2a and Mef2c genes, which are critical modulators of muscle differentiation and maturation in addition to Akt gene [29,30]. Our molecular analysis did not reveal significant differences in Mef2a expression levels between treated and untreated myoblasts in both control and G93A-SOD1 animals at any disease stage (Fig. 3A–C). We found an increase of Mef2c expression in 8-week G93A-SOD1 animal myoblasts under treatment compared to both control and G93A-SOD1 untreated cells and treated cells from 8-week control animals. This increase became significant for treated G93A-SOD1 myoblasts isolated at weeks 12 compared to the treated cells from 12-week control animals (Fig. 3A, B, $p < 0.05$), but not in untreated G93A-SOD1 cells compared to untreated control cells and in untreated compared to treated control cells.

3.4. Increased expression of energetic status-related genes in G93A-SOD1 myoblasts treated with FM19G11-loaded NPs

To determine whether the FM19G11-loaded NP treatment could affect the energetic status of G93A-SOD1 myoblasts, we evaluated the expression of Glut4 and Ucp2 genes in treated and untreated myoblasts from mice at different disease stages and control myoblasts. Glut4 is a glucose transporter critically implicated in glucose homeostasis and uptake into muscle cells, that is relevant to support the energetic requirement for the muscle activity [31], and with Akt gene act as antioxidant defense improving glucose homeostasis [32]. No significant difference was found in myoblast Glut4 mRNA levels before and after the treatment (Fig. 4A–C). However, we observed an increased expression, though not significant, of this gene in FM19G11-loaded NP-treated myoblasts from 18-weeks G93A-SOD1 mice compared to untreated

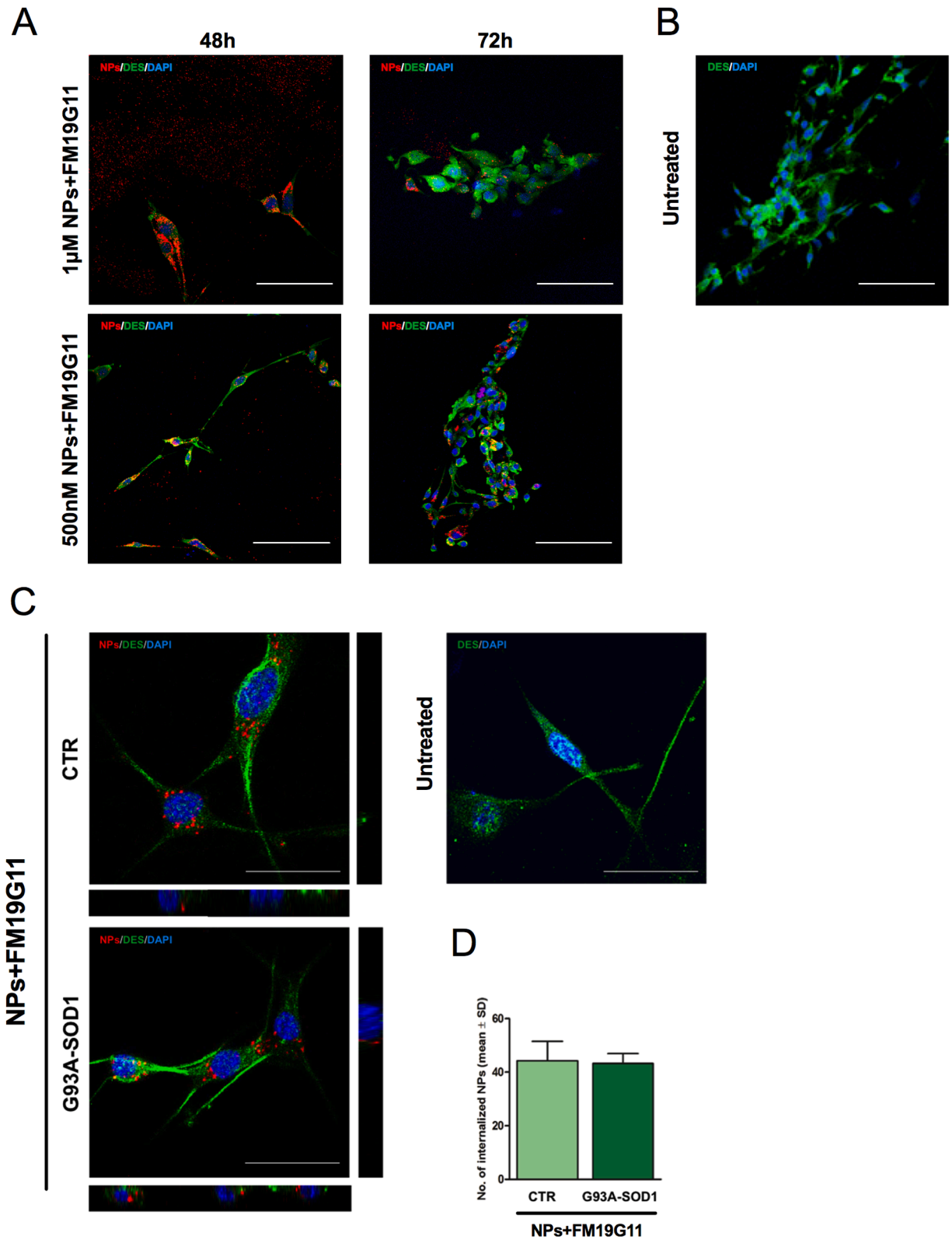

Fig. 1. Optimal FM19G11 treatment condition in myoblasts cells. A) Representative confocal images of myoblasts derived from G93A-SOD1 mice at week 18 of age treated with NPs+FM19G11 at 1 μM and 500 nM for 48 and 72 h. Cells were stained for desmin (DES, green), and co-stained with DAPI (blue) for cell nuclei. B) Representative confocal images of untreated myoblasts derived from G93A-SOD1 mice at week 18 of age. C) Representative confocal images of the orthogonal and sagittal projections showing the cytoplasmic localization of NPs+FM19G11 into myoblasts in both G93A-SOD1 and CTR myoblasts at week 18. Cells were stained for desmin (DES, green), and co-stained with DAPI (blue) for cell nuclei. D) Quantification of the number of the internalized NPs+FM19G11 in CTR and G93A-SOD1 myoblasts. The number of NPs was assessed in four different cultures per each group, with three images randomly acquired for each. The statistical analysis (Mann-Whitney, $p = 0.77$) was performed using FiJi-ImageJ software. Scale bar: 50μm.

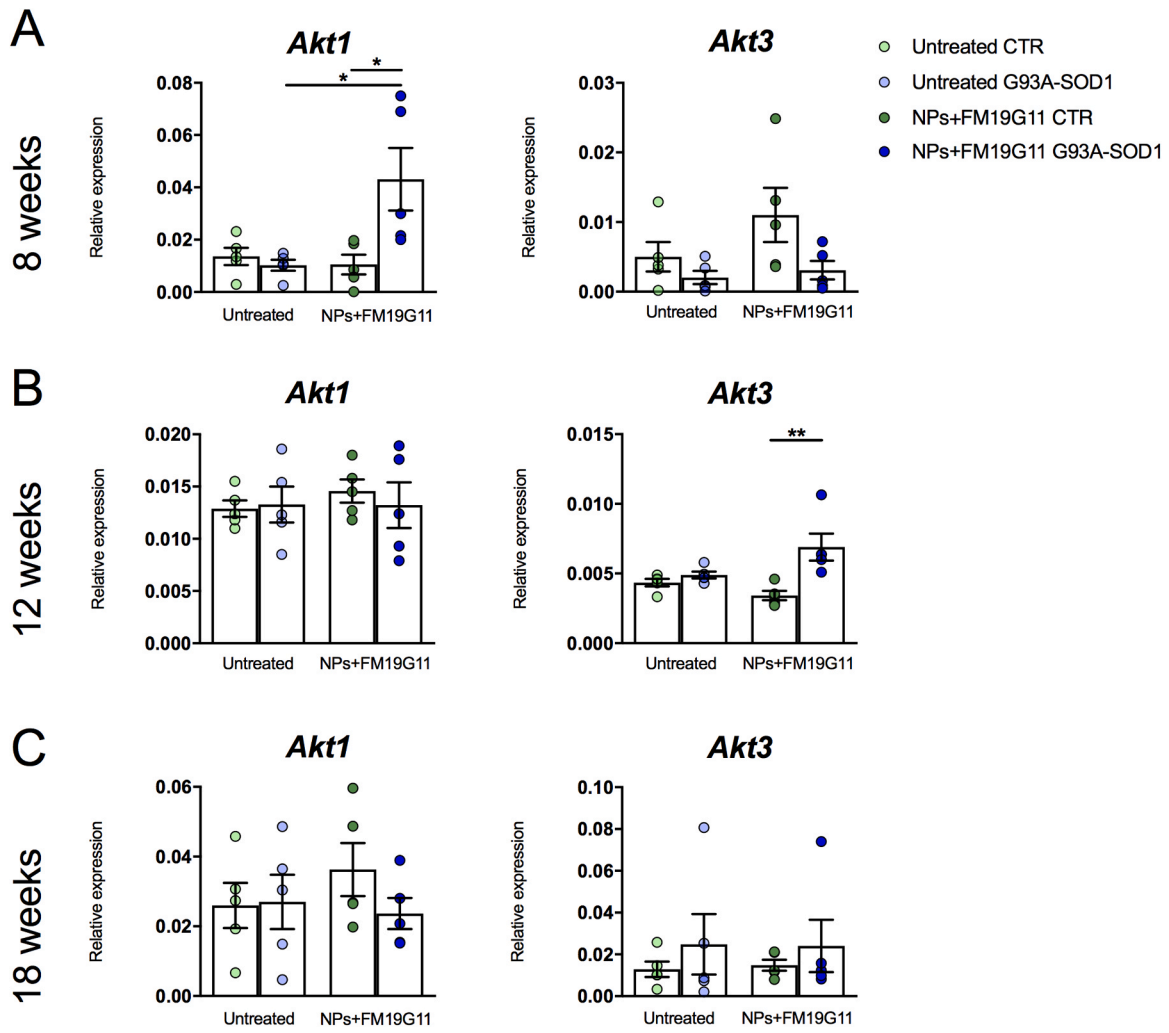

Fig. 2. Expression analysis of the proliferation markers Akt1 and Akt3 following FM19G11-loaded NP treatment. Quantitative real-time PCR analysis of the expression levels of Akt1 and Akt3 mRNAs in myoblasts from CTR (n = 5, green bars) and G93A-SOD1 (n = 5, blue bars) mice at weeks (A) 8 (presymptomatic disease stage), (B) 12 (disease onset), and (C) 18 (end stage of the disease) after 72 h of NPs+FM19G11 treatment (dashed bars) compared to untreated cells (full bars). Relative expression data are presented as mean ± SEM of $2^{-\Delta Ct}$ values normalized toward the endogenous control 18 S. * $p < 0.05$, **$p < 0.01$, Kruskall-Wallis test followed by Dunn analysis.

G93A-SOD1 and control cells, suggesting a potential ability of NP-linked FM19G11 to promote glucose uptake into muscle cells through Glut4 (Fig. 4C).

It has previously been demonstrated that FM19G11-loaded NP treatment can induce the expression of mitochondrial genes (e.g UCP1, UCP2) and sustain mitochondrial activity, thereby triggering an adaptive cellular response that increases ATP production [22].

Based on this evidence, we assessed the impact of the treatment on myoblast expression of Ucp2, a nuclear gene encoding for a mitochondrial uncoupling protein implicated in energy metabolism and ROS production [18]. Interestingly, we found that Ucp2 transcriptional levels were significantly upregulated in treated myoblasts from 18-weeks G93A-SOD1 mice compared to G93A-SOD1 untreated cells ($p < 0.05$) and to untreated and treated control cells (Fig. 4B, $p < 0.01$), but not in untreated G93A-SOD1 cells compared to untreated control cells and in untreated compared to treated control cells. These findings suggest FM19G11-loaded NPs capacity to affect mitochondrial activity via Ucp2 modulation in myoblasts of affected animals during disease progression as an attempt to counteract pathological events.

3.5. FM19G11-loaded NP treatment reduces mithocondrial area and networks in G93A-SOD1 myoblasts

To analyze the effects of FM19G11-loaded NP treatment on the dynamic cycle of mitochondrial fusion and fission, whose balance influences morphology and function of mitochondrial networks, we analyzed the mitochondrial networks in FM19G11-loaded NP-treated and untreated myoblasts isolated from control and G93A-SOD1 animals during disease progression (i.e. 8, 12, and 18 weeks). As shown in skeleton images (Fig. 5), the area occupied by mitochondria networks was larger in G93A-SOD1 than control cells at basal condition, suggesting that mitochondria from affected myoblasts may undergo increased fusion processes. Of note, this parameter appeared reduced in FM19G11-loaded NP-treated G93A-SOD1 myoblasts isolated at all the disease stages (Fig. 5).

This phenomenon was confirmed by quantitative analysis using MiNA (https://github.com/StuartLab) [25]. Indeed, in myoblasts isolated from mice at 8 and 12 weeks, we observed significantly higher values of the mitochondrial footprint parameter, which represents the mitochondrial area, in G93A-SOD1 compared to untreated control cells (Fig. 6A, $p < 0.01$, and Fig. 6B, $p < 0.0001$). These values underwent a decrease after FM19G11-loaded NP treatment in G93A-SOD1 cells

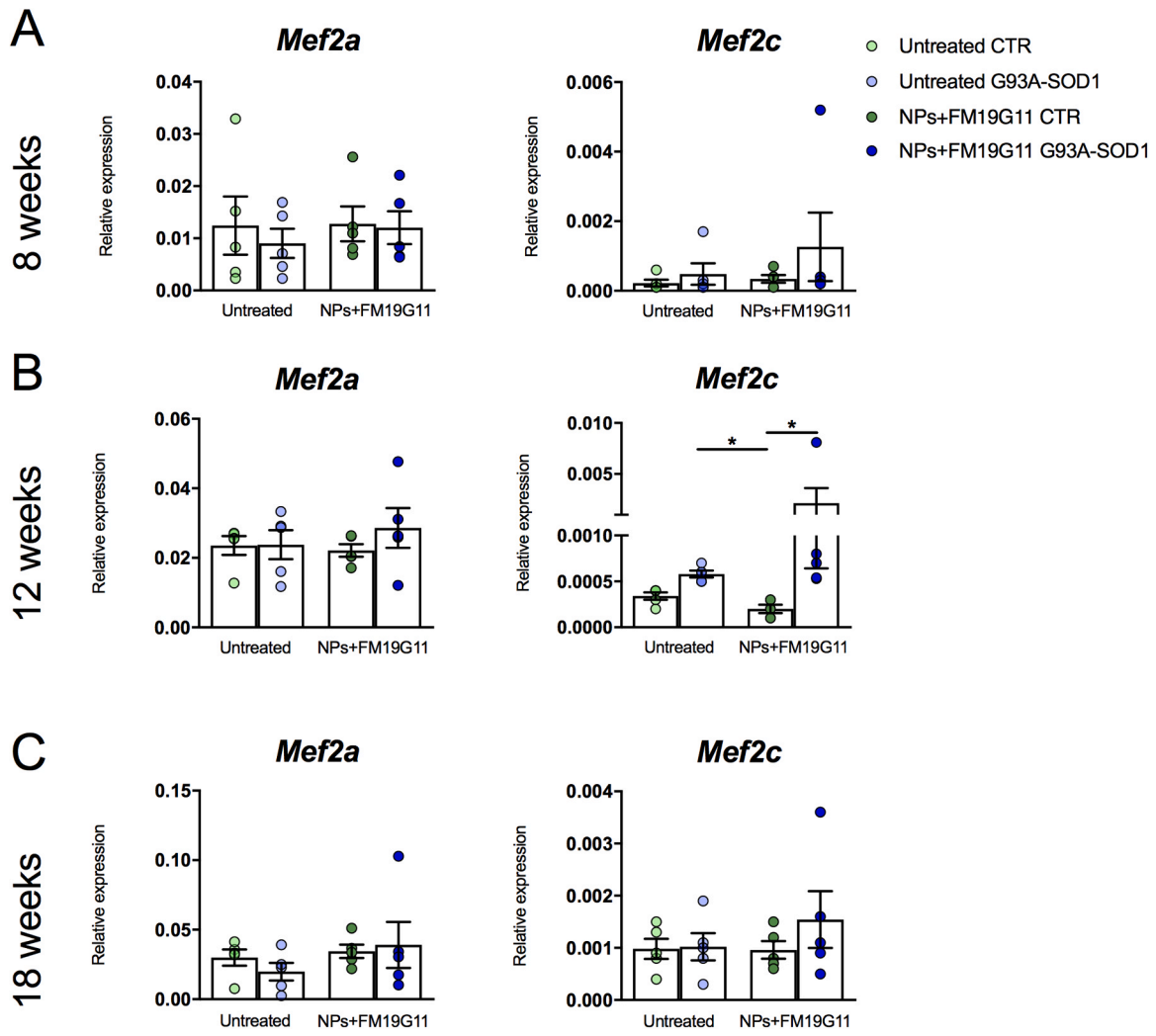

Fig. 3. Expression analysis of the muscle differentiation markers Mef2a and Mef2c following FM19G11-loaded NP treatment. Quantitative real-time PCR analysis of the expression levels of Mef2a and Mef2c mRNAs in myoblasts from CTR (n = 5, green bars) and G93A-SOD1 (n = 5, blue bars) mice at weeks (A) 8 (presymptomatic disease stage), (B) 12 (disease onset), and (C) 18 (end stage of the disease) after 72 h of NPs+FM19G11 treatment (dashed bars) compared to untreated cells (full bars). Relative expression data are presented as mean ± SEM of $2^{-\Delta Ct}$ values normalized toward the endogenous control 18 S. * $p < 0.05$, Kruskall-Wallis test followed by Dunn analysis.

(Fig. 6A, $p < 0.01$ and Fig. 6B, $p < 0.0001$). No significant differences were observed at week 18 (Fig. 6C).

Regarding the architectural composition of mitochondrial networks, we found a significantly higher number of mitochondrial networks, but not of individual mitochondria, in myoblasts isolated from 18-week G93A-SOD1 mice compared to control cells at basal condition (Fig. 6C, $p < 0.001$). Of note, the number of these networks significantly decreased in the same cells under treatment compared to the untreated cells, thus suggesting FM19G11-loaded NP ability to rimodel the mitochondrial networks (Fig. 6C, $p < 0.05$). Moreover, the number of both individual and network mitochondria was lower in 12-week G93A-SOD1 myoblasts under treatment compared to treated control cells (Fig. 6B, $p < 0.0001$, and $p < 0.001$). We also assessed the size of the mitochondrial networks. Interestingly, network size was significantly higher in both 12- and 18-week G93A-SOD1 compared to control myoblasts at basal condition (Fig. 6B, $p < 0.0001$, and C $p < 0.001$). The size was significantly reduced in G93A-SOD1 cells under FM19G11-loaded NP treatment compared to the untreated cells (Fig. 6B, $p < 0.0001$, and C $p < 0.05$), indicating an effect of the treatment on mitochondrial networks. The analysis of the mean branch lenght parameter, which is indicative of the extension of the mitochondrial networks, displayed a significant increase in 8-week control myoblasts compared to 8-week G93A-SOD1 untreated mouse cells and treated control cells (Fig. 6A, $p < 0.01$, $p < 0.05$). Contrariwise, mean branch lenght was significantly higher in 12-week G93A-SOD1 cells compared to controls at basal condition (Fig. 6B, $p < 0.0001$), but decreased after FM19G11-loaded NP treatment (Fig. 6B, $p < 0.0001$).

3.6. ROS production is reduced in G93A-SOD1 myoblasts treated with FM19G11-loaded NPs

To evaluate the effect of FM19G11-loaded NPs on oxidative stress, we assessed the producion of ROS in treated and untreated myoblasts from 8-, 12- and 18-week G93A-SOD1 and control mice by specific ROS staining with CellROX. We did not observe ROS production in cells from both disease and control animals at 8 and 12 weeks (data not shown). In contrast, myoblasts from 18-week G93A-SOD1 mice at basal condition showed a strong positive signal compared to cells isolated from control mice at the same week (Fig. 7A), in line with ROS accumulation during disease progression. Of note, this signal was significantly reduced by the treatment with FM19G11-loaded NPs, as demonstrated by quantitive analysis of CellROX-positive fields in treated compared to untreated G93A-SOD1 myoblast cultures (Fig. 7A and B, $p < 0.01$). These data suggest that FM19G11-loaded NPs are able to rescue oxidative stress in

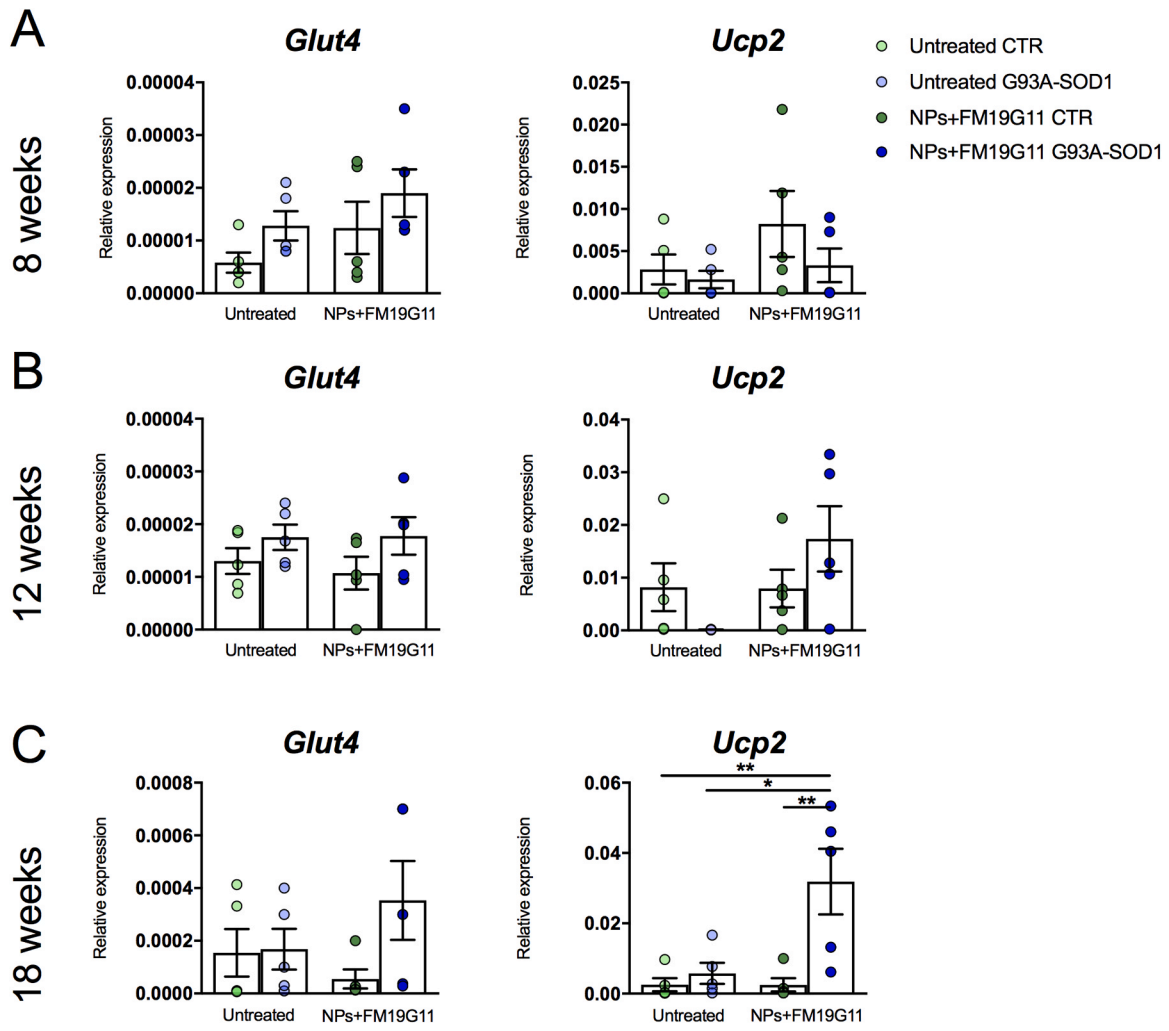

Fig. 4. Expression analysis of the energetic status-related markers Glut4 and Ucp2 following FM19G11-loaded NP treatment. Quantitative real-time PCR analysis of the expression levels of Glut4 and Ucp2 mRNAs in myoblasts from CTR (n = 5, green bars) and G93A-SOD1 (n = 5, blue bars) mice at weeks (A) 8 (presymptomatic disease stage), (B) 12 (disease onset), and (C) 18 (end stage of the disease) after 72 h of NPs+FM19G11 treatment (dashed bars) compared to untreated cells (full bars). Relative expression data are presented as mean ± SEM of $2^{-\Delta Ct}$ values normalized toward the endogenous control 18 S. * $p < 0.05$, **$p < 0.01$, Kruskall-Wallis test followed by Dunn analysis.

G93A-SOD1 myoblasts as disease progresses.

4. Discussion

The underpinning pathogenic mechanisms in ALS are complex and multifaceted. Despite decades of intensive research, the understanding of the exact causative processes remains elusive. The FDA-approved treatments, riluzole, edaravone, sodium phenylbutyrate-taurursodiol and tofersen, each act on a specific ALS pathogenic mechanism, *i.e.* glutamate excitotoxicity, oxidative stress, nerve cell death, and SOD1 aggregates, respectively, although with poor clinically meaningful effectiveness [33]. This suggests that a plethora of alterations, rather than a single event, operate simultaneously to trigger the disease, and that ALS pathogenesis is beyond a cell autonomous mechanism of the central nervous system [34]. Hence, alternative treatment strategies need to be explored to address a combination of molecular targets and pathways for a synergistic therapeutic effect. Growing evidence suggests that muscle alterations could play a crucial role in triggering the disease [4], and indicates that the muscle could be a promising therapeutic target to improve muscle tissue homeostasis and function, which, in turn, would lead to an increased survival of motor neurons due to the strict 'motor neuron–muscle' interplay [5].

The present study aimed to investigate the effect of FM19G11 on cell proliferation, energetic status, and ROS production in myoblasts derived from muscle tissue of G93A-SOD1 mice at different disease stages. Based on our previous data regarding the enhancement of FM19G11 effect when delivered with NP formulations [23], and to improve the translational applicability of our findings, we delivered the FM19G11 into myoblasts with biodegradable PLGA NPs.

Of note, the nanoformulation is based on PLGA, a biodegradable polymer that has been extensively studied as nanocarrier on a vast group of cells. PLGA NPs have been fully characterized and validated, earning widespread recognition [35]. PLGA hydrolysis produces metabolite monomers that are endogenous and easily metabolized by the body through the Krebs cycle, resulting in minimal systemic toxicity associated with the use of PLGA for drug delivery or biomaterial applications [36]. Furthermore, PLGA has been approved by both the US FDA and the European

Medicine Agency (EMA) for various drug delivery systems in humans. Based on this evidence and previous studies, the PLGA nanosystem is not toxic but shows an excellent biocompatibility and biodegradability [24,37]. Although we did not test the molecular and cellular effects of PLGA alone, that is a limitation of our study, we are confident that the observed results were due to the FM19G11 action. Indeed, it was

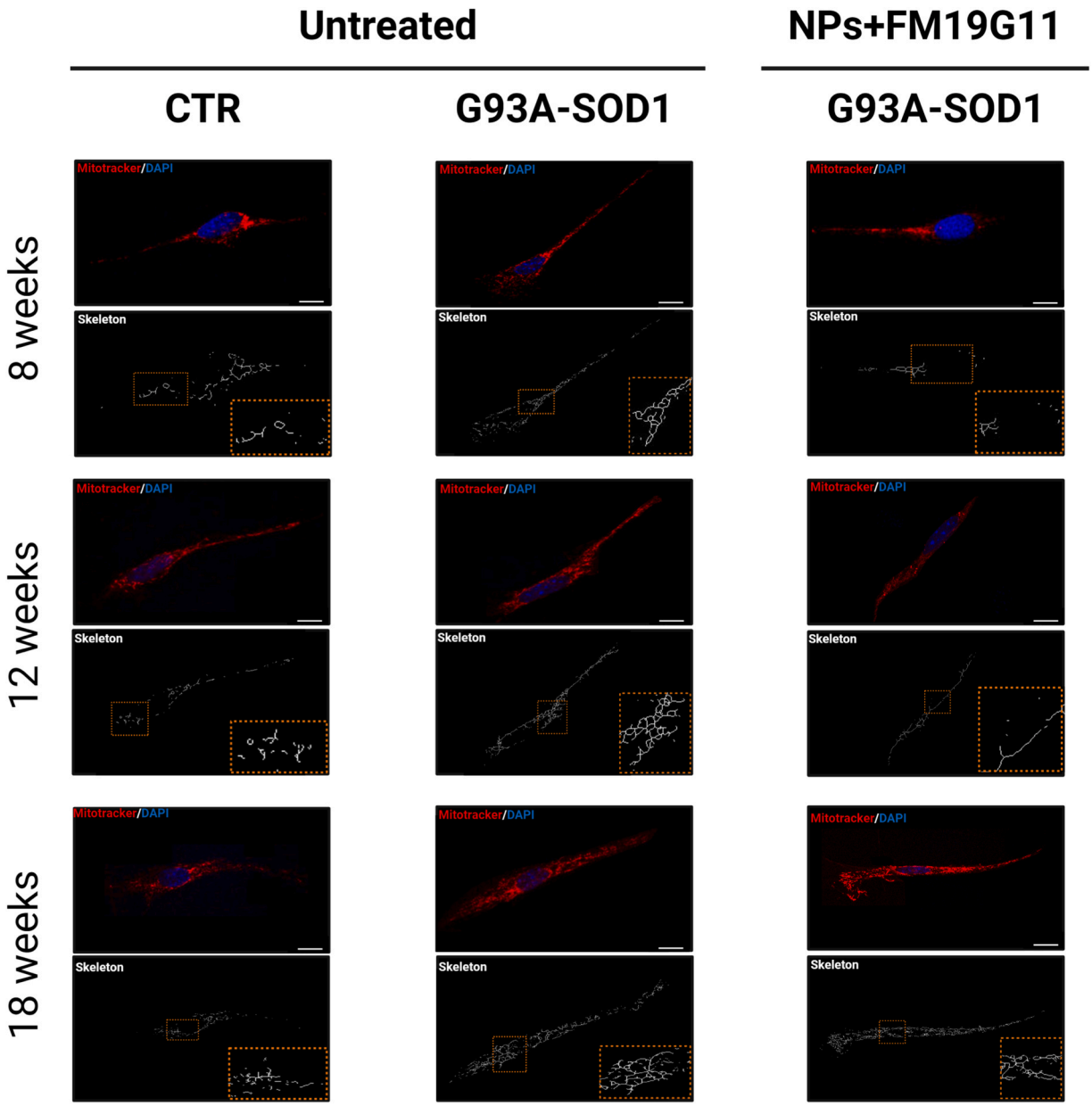

Fig. 5. Representative confocal images of mitochondrial network morphology following FM19G11-loaded NP treatment. Representative confocal images of untreated myoblasts derived from CTR and G93A-SOD1 mice at 8, 12, 18 weeks of age (left panel) and after FM19G11-loaded NPs (right panel). Cells were stained with Mitotracker orange (red) and co-stained with DAPI (blue) for cell nuclei. Skeleton images (white) obtained by MiNA toolset for the mitochondrial network morphology quantification. Scale bar = 10 μm. The inserts correspond to an enlargement of the skeleton images in the area close to the nuclei, 300x magnification.

demostrated that the empty PLGA did not influence cell prolifelation and survival [38] or cellular signaling pathways, and it did not display therapeutic effects in different disease contexts, such as tumors [39] or cardic remodeling [40]. Of note, several nanotherapeutics are under investigation in phase II and phase III clinical trials. Results of these trials are promising if we consider that nanotechnology-based strategies employ engineered nanovectors that are able to deliver single or combined therapeutic agents into the cells, allowing to overcome biological barriers, enhance interaction with targeted sites, improve drug bioavailability/bio-stability, and minimize systemic side-effects [41].

Herein, we first assessed the effect of FM19G11-loaded NP treatment on muscle cell proliferation by the analysis of AKT genes, specifically the Akt1/PKBα and Akt3/PKBγ isoforms that are expressed in skeletal muscle and positively regulate cell growth by counteracting apoptotic pathways [42–44]. A previous study demonstrated a link between reduction of AKT expression and alterations of the muscle fiber size in several animal models of muscle wasting and ALS patients [28]. Abnormalities in mitochondrial biogenesis, function, and morphology have also been correlated with reduced AKT expression, thus highlighting the critical role of this gene in maintaining skeletal muscle metabolism and oxidative capacity [28]. In addition, it has been shown that Akt3 gene promotes C2C12 proliferation and delays their differentiation [45,46]. Our molecular analyses revealed Akt1 and Akt3 upregulation in myoblasts from G93A-SOD1 mice at the pre-symptomatic and onset stages of disease following FM19G11-loaded NP treatment, disclosing a positive impact of FM19G11 on myoblast proliferation that could influence the muscle remodeling in response to the disease-associated atrophy. In cells representative of the end stage of the disease (myoblasts isolated from mice at 18 weeks), we did not observe an effect of FM19G11 on the PI3K/AKT activation cell survival pathway, probably due to the massively compromised metabolism caused by SOD1 aggregations, in line with what we have previously observed in NPCs [23].

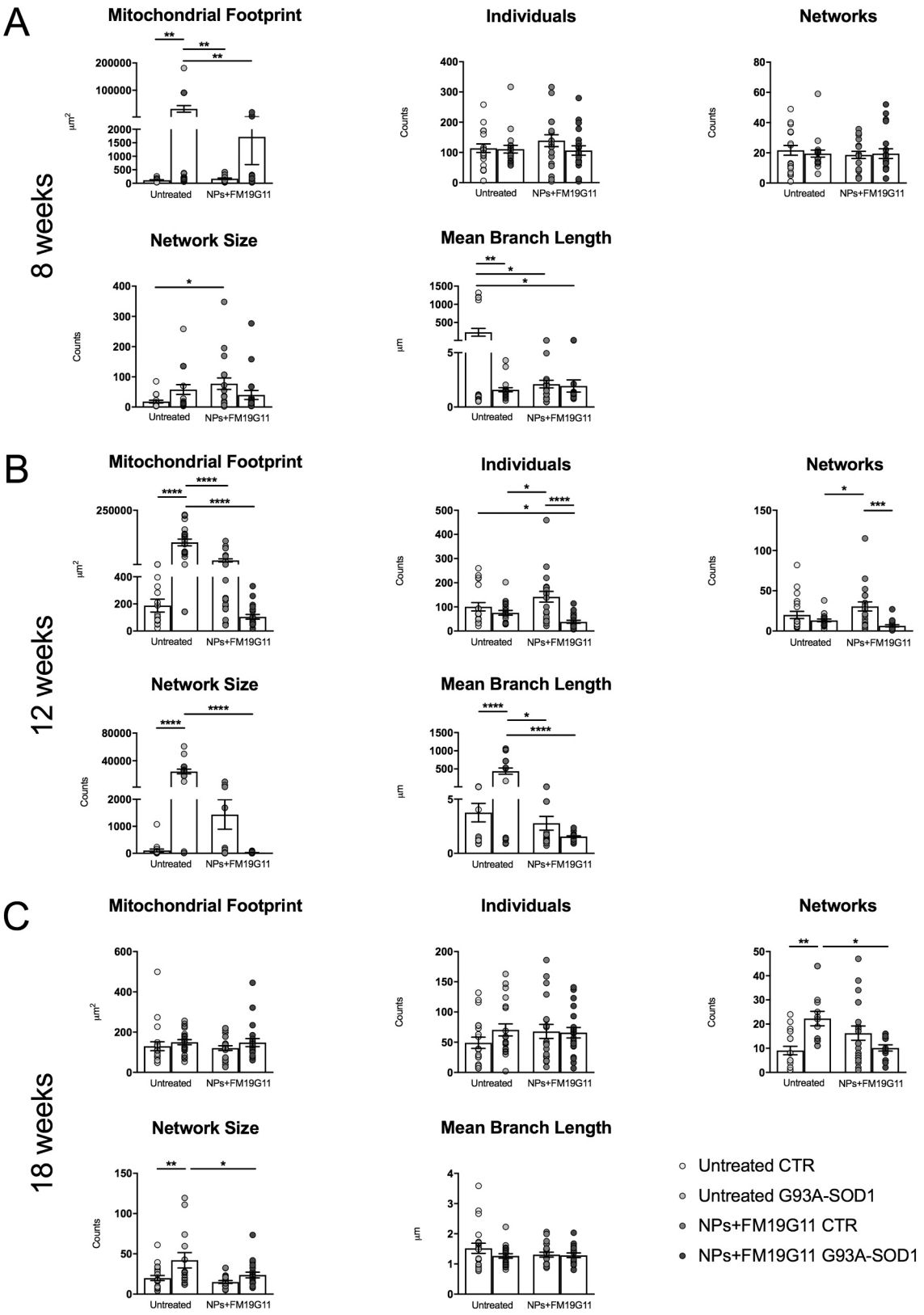

Fig. 6. Quantification of mitochondrial network morphology in control and G93A-SOD1 myoblasts following FM19G11-loaded NP treatment. MiNA output including mitochondrial footprint, individuals, networks, network size and mean branch length, from myoblasts derived from CTR (green bars) and G93A-SOD1 (blue bars) mice (three mice per group) at (A) 8 (presymptomatic disease stage), (B) 12 (disease onset), and (C) 18 (symptomatic stage of the disease) weeks after 72 h of FM19G11-loaded NP treatment (dashed bars) compared to untreated cells (full bars). Mitotracker staining was analyzed in seven cells per coverslip for one culture per condition. The statistical analysis was performed using Fiji-ImageJ software. Data are represented as mean ± SEM. * $p < 0.05$, ** $p < 0.01$, **** $p < 0,0001$, Kruskall-Wallis test followed by Dunn analysis.

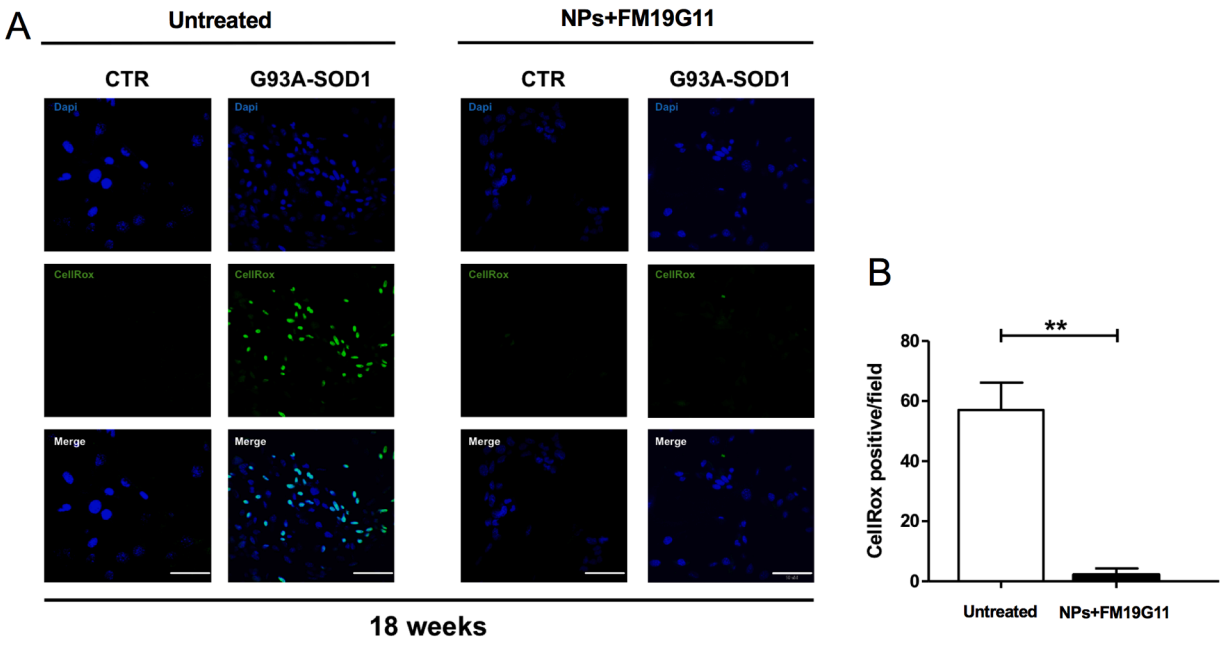

Fig. 7. ROS production analysis in G93A-SOD1 myoblasts following FM19G11-loaded NP treatment. (A) Representative confocal images of CellROX (green) staining in CTR and G93A-SOD1 myoblasts at week 18 after 72 h of FM19G11-loaded NP treatment compared to untreated cells. The CellROX stained displays the production of ROS in untreated (Basal) and treated cells. Green foci represent CellROX dye upon oxidation by ROS and binding to DNA (blue). (B) Quantitative analysis of CellROX-positive cells in basal (white bars) and FM19G11-loaded NP treated (black bars) G93A-SOD1 myoblasts. No positive signal was observed in myoblasts from control mice. CellROX staining was performed in three cultures per group and 30 cells per condition were quantified. The statistical analysis (Mann-Whitney, $p = 0.0043$) was performed using FiJi-ImageJ software. Data are represented as mean ± SEM. ** $p < 0.01$, Mann-Whitney test. Scale bar = 50 μm.

To better understand the molecular events underlying muscle cell development upon FM19G11 treatment, we analyzed Mef2a and Mef2c expression in untreated and treated myoblasts, since these genes are critical modulators of myogenesis known to be overexpressed in response to muscle injury [29]. Specifically, Mef2a is activated in the early stage of muscle differentiation and its knockdown inhibits myoblast proliferation and differentiation [29], and Mef2c is involved in fiber type control and glucose uptake metabolism [47]. Our data showed an increase expression of Mef2c in G93A-SOD1 myoblasts after FM19G11-loaded NP treatment compared to untreated cells. This observation supported an effect of FM19G11 on muscle metabolism, thus highlighting possible application of this molecule in therapeutic approaches aimed at stimulating myogenesis to delay disease progression in ALS patients. Our molecular results are in line with data showing that the PI3K/Akt signaling pathway positively regulates Mef2c gene expression in different cell types and tissues, including skeletal muscle [48], further supporting FM19G11 ability to simultaneously activate the expression of Akt and hence Mef2c thus promoting myogenesis.

It is widely known that the UCP decoupling proteins exert a neuroprotective effect in ALS, and that UCP2 protein activation significantly correlates with ROS reduction in the mitochondria of neuronal cells [19]. Notably, our analysis unequivocally demonstrated a significant increase of UCP2 expression levels in G93A-SOD1 myoblasts isolated from mice at late disease stage after treatment with FM19G1-loaded NPs compared to untreated cells, suggesting the ability of FM19G11 to improve mitochondrial activity and protect G93A-SOD1 myoblasts via modulation of UCP2.

Of note, the effects of FM19G1-loaded NP treatment on the expression of the above genes are specifically observed in myoblasts of diseased, but not control, animals, indicating an attempt to counteract ALS-associated events in the pathological context in which the treatment acts. Although the FM19G1-loaded NP-induced changes do not correspond to a normalization of disease-associated alterations, they may have beneficial effects in terms of muscle function and energetic status improvement.

Since mitochondria alterations have a central role in the ALS pathogenesis [49] and FM19G11 is known to be a modulator of the mitochondrial metabolisms [22], we performed a mitochondrial network analysis in G93A-SOD1 and control myoblasts upon FM19G11 treatment, to evaluate the effect of the drug on mitochondrial network morphology. We revealed a significant increase of mitochondrial area, in terms of mitochondrial footprint and network size, in G93A-SOD1 myoblasts compared to control cells at basal condition. In line with these findings, it is widely described that oxidative stress, accumulation of proteins, excitotoxicity, and apoptosis cause abnormalities in mitochondrial morphology, resulting in the formation of mega-mitochondria, which are typically observed in ALS mice [50] and "bizarre giant mitochondria" identified in liver biopsies from ALS patients [47]. The ALS muscle mainly suffers from mitochondrial dysfunctions, oxidative stress, and bioenergetic disturbances [7,51]. Mitochondrial changes negatively affect myogenic processes, thereby altering cellular respiration rate and ATP production, leading to calcium homeostasis loss, stimulation of pro-apoptotic signaling and increased ROS levels [51–53]. Based on these observations, mitochondrial alterations are relevant in ALS pathogenesis, and proteins or mechanisms modulating their metabolism could be targets for therapeutic interventions. Of note, our results demonstrated a significant reduction of mitochondrial network area in myoblasts of G93A-SOD1 after FM19G11-loaded NP treatment. This reduction was associated with an increased expression of Akt and Ucp2 genes in G93A-SOD1 myoblasts, supporting the idea that FM19G11 may promote the restoring of disease-associated mitocondrial alterations *via* the activation of Akt and Ucp2 signalling pathways. As known, AKT, as well UCP2 gene [19], is a key regulator of mitophagy being a crucial modulator of mitochondria-mediated apoptosis, redox states, dynamic balance, autophagy, and metabolism [54].

By immunofluorescence analysis, we confirmed the impact of FM19G11 on the reduction of ROS production in G93A-SOD1 myoblasts. Indeed, we observed a positive signal for ROS in G93A-SOD1 cells isolated from mice at symptomatic phase of disease, that was significant

reduced after FM19G11-loaded NP treatment. Notably, ALS-associated muscle decline in mass, function, and reparative capacity is associated with high levels of ROS that reduce myoblast differentiation and increase apoptosis, causing poor muscle repair [55]. In ALS patients [56] and mice [57], ROS production plays a key role in the disease pathophysiology already at early stages. In addition, overexpression of ALS-causing mutation $SOD1^{G93A}$ in skeletal muscle of control mice was found to lead to similar abnormalities in mitochondrial network and dynamics, and boost mitochondrial ROS production [13]. Thus, the ability of FM19G11 to modulate mitochondrial function in ALS mouse cells suggests its potential application in therapeutic approaches aimed at delaying disease progression in ALS patients.

SOD1-ALS accounts for only $< 2\%$ of human ALS, and appears to be a possible outlier in the complex ALS landscape [58]. Thus, ALS therapies developed and tested in SOD1 transgenic animals, could not be applicable to patients with different ALS subtypes. Further studies aimed at testing FM19G11 treatment efficacy on cell metabolism and energetic status in other ALS models are needed to corroborate our data.

5. Conclusion

By highlighting the potential of FM19G11 as a novel skeletal muscle-targeting drug to counteract key disease-associated mechanisms, our overall findings promise to open new research avenues towards translation of FM19G11-based nanotherapies in the ALS. Based on the FM19G11 effects on muscle health these therapies could represent an innovative approach, to be explored, to slow muscle degeneration in the frame of muscle disorders.

Funding

This work was supported by: the Italian Ministry of Health (RRC); Fondazione Regionale per la Ricerca Biomedica POR FESR 2014—2020 under INTERSLA project, ID 1157625 (G.L.); CALabria HUB per Ricerca Innovativa ed Avanzata- CALHUB.RIA “Creazione di Hub delle Scienze della Vita” T4-AN-09 prog. ZRPOS2.

CRediT authorship contribution statement

Silvia Bonanno: Writing – review & editing, Conceptualization. **Cristina Chirizzi:** Writing – original draft, Resources, Methodology, Investigation, Conceptualization. **Marco Cattaneo:** Investigation, Formal analysis. **Fulvia Saraceno:** Investigation, Formal analysis. **Paola Cavalcante:** Writing – review & editing. **Giuseppe Lauria:** Supervision, Funding acquisition. **Pierangelo Metrangolo:** Writing – review & editing, Supervision, Funding acquisition. **Claudia Malacarne:** Writing – original draft, Visualization, Methodology, Formal analysis, Data curation, Conceptualization. **Francesca Baldelli Bombelli:** Writing – review & editing, Supervision, Project administration, Methodology, Conceptualization, Funding acquisition. **Eleonora Giagnorio:** Writing – original draft, Visualization, Validation, Software, Investigation, Formal analysis, Data curation, Conceptualization. **Stefania Marcuzzo:** Writing – original draft, Visualization, Methodology, Funding acquisition, Data curation, Conceptualization. **Renato Mantegazza:** Supervision, Project administration. **Victoria Moreno-Manzano:** Writing – review & editing, Resources.

Declaration of Competing Interest

The authors report no competing interests.

Data Availability

Data will be made available on request.

Appendix A. Supporting information

Supplementary data associated with this article can be found in the online version at doi:10.1016/j.biopha.2024.116380.

References

[1] D.R. Rosen, T. Siddique, D. Patterson, D.A. Figlewicz, P. Sapp, A. Hentati, D. Donaldson, J. Goto, J.P. O'Regan, H.X. Deng, Mutations in Cu/Zn superoxide dismutase gene are associated with familial amyotrophic lateral sclerosis, Nature 362 (6415) (1993) 59–62.
[2] X. Xu, D. Shen, Y. Gao, Q. Zhou, Y. Ni, H. Meng, H. Shi, W. Le, S. Chen, A perspective on therapies for amyotrophic lateral sclerosis: can disease progression be curbed? Transl. Neurodegener. 10 (1) (2021) 29.
[3] F. Kreilaus, S. Guerra, R. Masanetz, V. Menne, J. Yerbury, T. Karl, Novel behavioural characteristics of the superoxide dismutase 1 G93A (SOD1, Genes Brain Behav. 19 (2) (2020) e12604.
[4] S. Marcuzzo, I. Zucca, A. Mastropietro, N.K. de Rosbo, P. Cavalcante, S. Tartari, S. Bonanno, L. Preite, R. Mantegazza, P. Bernasconi, Hind limb muscle atrophy precedes cerebral neuronal degeneration in G93A-SOD1 mouse model of amyotrophic lateral sclerosis: a longitudinal MRI study, Exp. Neurol. 231 (1) (2011) 30–37.
[5] E. Giagnorio, C. Malacarne, R. Mantegazza, S. Bonanno, S. Marcuzzo, MyomiRs and their multifaceted regulatory roles in muscle homeostasis and amyotrophic lateral sclerosis, J. Cell Sci. 134 (12) (2021).
[6] M. Wong, L.J. Martin, Skeletal muscle-restricted expression of human SOD1 causes motor neuron degeneration in transgenic mice, Hum. Mol. Genet. 19 (11) (2010) 2284–2302.
[7] J.P. Loeffler, G. Picchiarelli, L. Dupuis, J.L. Gonzalez De Aguilar, The role of skeletal muscle in amyotrophic lateral sclerosis, Brain Pathol. 26 (2) (2016) 227–236.
[8] V. Crugnola, C. Lamperti, V. Lucchini, D. Ronchi, L. Peverelli, A. Prelle, M. Sciacco, A. Bordoni, E. Fassone, F. Fortunato, S. Corti, V. Silani, N. Bresolin, S. Di Mauro, G. P. Comi, M. Moggio, Mitochondrial respiratory chain dysfunction in muscle from patients with amyotrophic lateral sclerosis, Arch. Neurol. 67 (7) (2010) 849–854.
[9] G. Luo, J. Yi, C. Ma, Y. Xiao, F. Yi, T. Yu, J. Zhou, Defective mitochondrial dynamics is an early event in skeletal muscle of an amyotrophic lateral sclerosis mouse model, PLoS One 8 (12) (2013) e82112.
[10] J. Zhou, J. Yi, R. Fu, E. Liu, T. Siddique, E. Ríos, H.X. Deng, Hyperactive intracellular calcium signaling associated with localized mitochondrial defects in skeletal muscle of an animal model of amyotrophic lateral sclerosis, J. Biol. Chem. 285 (1) (2010) 705–712.
[11] Y. Xiao, C. Ma, J. Yi, S. Wu, G. Luo, X. Xu, P.H. Lin, J. Sun, J. Zhou, Suppressed autophagy flux in skeletal muscle of an amyotrophic lateral sclerosis mouse model during disease progression, Physiol. Rep. 3 (1) (2015).
[12] R.S. Balaban, S. Nemoto, T. Finkel, Mitochondria, oxidants, and aging, Cell 120 (4) (2005) 483–495.
[13] Y. Xiao, C. Karam, J. Yi, L. Zhang, X. Li, D. Yoon, H. Wang, K. Dhakal, P. Ramlow, T. Yu, Z. Mo, J. Ma, J. Zhou, ROS-related mitochondrial dysfunction in skeletal muscle of an ALS mouse model during the disease progression, Pharm. Res. 138 (2018) 25–36.
[14] A. Ledesma, M.G. de Lacoba, E. Rial, The mitochondrial uncoupling proteins, Genome Biol. 3 (12) (2002). REVIEWS3015.
[15] P. Schrauwen, M. Hesselink, UCP2 and UCP3 in muscle controlling body metabolism, J. Exp. Biol. 205 (Pt 15) (2002) 2275–2285.
[16] P.W. Ho, J.W. Ho, H.F. Liu, D.H. So, Z.H. Tse, K.H. Chan, D.B. Ramsden, S.L. Ho, Mitochondrial neuronal uncoupling proteins: a target for potential disease-modification in Parkinson's disease, Transl. Neurodegener. 1 (1) (2012) 3.
[17] F. Bartolome, H.C. Wu, V.S. Burchell, E. Preza, S. Wray, C.J. Mahoney, N.C. Fox, A. Calvo, A. Canosa, C. Moglia, J. Mandrioli, A. Chiò, R.W. Orrell, H. Houlden, J. Hardy, A.Y. Abramov, H. Plun-Favreau, Pathogenic VCP mutations induce mitochondrial uncoupling and reduced ATP levels, Neuron 78 (1) (2013) 57–64.
[18] S. Cadenas, Mitochondrial uncoupling, ROS generation and cardioprotection, Biochim. Biophys. Acta Bioenerg. 1859 (9) (2018) 940–950.
[19] Z.B. Andrews, S. Diano, T.L. Horvath, Mitochondrial uncoupling proteins in the CNS: in support of function and survival, Nat. Rev. Neurosci. 6 (11) (2005) 829–840.
[20] M. Hoffmann, Enhanced uncoupling of the mitochondrial respiratory chain as a potential source for amyotrophic lateral sclerosis, Front. Neurol. 4 (2013) 86.
[21] V. Moreno-Manzano, F.J. Rodríguez-Jiménez, J.L. Aceña-Bonilla, S. Fustero-Lardíes, S. Erceg, J. Dopazo, D. Montaner, M. Stojkovic, J.M. Sánchez-Puelles, FM19G11, a new hypoxia-inducible factor (HIF) modulator, affects stem cell differentiation status, J. Biol. Chem. 285 (2) (2010) 1333–1342.
[22] F.J. Rodríguez-Jimnez, A. Alastrue-Agudo, S. Erceg, M. Stojkovic, V. Moreno-Manzano, FM19G11 favors spinal cord injury regeneration and stem cell self-renewal by mitochondrial uncoupling and glucose metabolism induction, Stem Cells 30 (10) (2012) 2221–2233.
[23] S. Marcuzzo, D. Isaia, S. Bonanno, C. Malacarne, P. Cavalcante, A. Zacheo, V. Laquintana, N. Denora, B. Sanavio, E. Salvati, P. Andreozzi, F. Stellacci, S. Krol, M. Mellado-López, R. Mantegazza, V. Moreno-Manzano, P. Bernasconi, FM19G11-loaded gold nanoparticles enhance the proliferation and self-renewal of ependymal stem progenitor cells derived from ALS mice, Cells 8 (3) (2019).
[24] C. Chirizzi, L. Gatti, M. Sancho-Albero, V. Sebastian, M. Arruebo, L. Uson, G. Neri, J. Santamaria, P. Metrangolo, L. Chaabane, F. Baldelli Bombelli, Optimization of

superfluorinated PLGA nanoparticles for enhanced cell labelling and detection by, Colloids Surf. B Biointerfaces 220 (2022) 112932.
[25] A.J. Valente, L.A. Maddalena, E.L. Robb, F. Moradi, J.A. Stuart, A simple ImageJ macro tool for analyzing mitochondrial network morphology in mammalian cell culture, Acta Histochem. 119 (3) (2017) 315–326.
[26] E.F. Iannetti, J.A. Smeitink, J. Beyrath, P.H. Willems, W.J. Koopman, Multiplexed high-content analysis of mitochondrial morphofunction using live-cell microscopy, Nat. Protoc. 11 (9) (2016) 1693–1710.
[27] R.A. McCloy, S. Rogers, C.E. Caldon, T. Lorca, A. Castro, A. Burgess, Partial inhibition of Cdk1 in G 2 phase overrides the SAC and decouples mitotic events, Cell Cycle 13 (9) (2014) 1400–1412.
[28] N. Jaiswal, M. Gavin, E. Loro, J. Sostre-Colón, P.A. Roberson, K. Uehara, N. Rivera-Fuentes, M. Neinast, Z. Arany, S.R. Kimball, T.S. Khurana, P.M. Titchenell, AKT controls protein synthesis and oxidative metabolism via combined mTORC1 and FOXO1 signalling to govern muscle physiology, J. Cachex-.-. Sarcopenia Muscle 13 (1) (2022) 495–514.
[29] N. Liu, B.R. Nelson, S. Bezprozvannaya, J.M. Shelton, J.A. Richardson, R. Bassel-Duby, E.N. Olson, Requirement of MEF2A, C, and D for skeletal muscle regeneration, Proc. Natl. Acad. Sci. U. S. A. 111 (11) (2014) 4109–4114.
[30] E.M. Wilson, J. Tureckova, P. Rotwein, Permissive roles of phosphatidyl inositol 3-kinase and Akt in skeletal myocyte maturation, Mol. Biol. Cell 15 (2) (2004) 497–505.
[31] T. Wang, J. Wang, X. Hu, X.J. Huang, G.X. Chen, Current understanding of glucose transporter 4 expression and functional mechanisms, World J. Biol. Chem. 11 (3) (2020) 76–98.
[32] V. Ramachandran, R. Saravanan, Glucose uptake through translocation and activation of GLUT4 in PI3K/Akt signaling pathway by asiatic acid in diabetic rats, Hum. Exp. Toxicol. 34 (9) (2015) 884–893.
[33] T.M. Miller, M.E. Cudkowicz, A. Genge, P.J. Shaw, G. Sobue, R.C. Bucelli, A. Chiò, P. Van Damme, A.C. Ludolph, J.D. Glass, J.A. Andrews, S. Babu, M. Benatar, C. J. McDermott, T. Cochrane, S. Chary, S. Chew, H. Zhu, F. Wu, I. Nestorov, D. Graham, P. Sun, M. McNeill, L. Fanning, T.A. Ferguson, S. Fradette, V.a.O.W. Group, Trial of antisense oligonucleotide tofersen for, N. Engl. J. Med. 387 (12) (2022) 1099–1110.
[34] J.P. Taylor, R.H. Brown, D.W. Cleveland, Decoding ALS: from genes to mechanism, Nature 539 (7628) (2016) 197–206.
[35] F. Danhier, E. Ansorena, J.M. Silva, R. Coco, A. Le Breton, V. Préat, PLGA-based nanoparticles: an overview of biomedical applications, J. Control Release 161 (2) (2012) 505–522.
[36] M. Kumari, S. Chaudhary, Modulating the physicochemical and biological properties of carbon dots synthesised from plastic waste for effective sensing of E. coli, Colloids Surf. B Biointerfaces 196 (2020) 111333.
[37] K.Hirenkumar Makadia, S.J. Siegel, Poly lactic-co-glycolic acid (PLGA) as biodegradable controlled drug delivery carrier, Polym. (Basel) 3 (3) (2011) 1377–1397.
[38] T. Latronico, F. Rizzi, A. Panniello, V. Laquintana, I. Arduino, N. Denora, E. Fanizza, S. Milella, C.M. Mastroianni, M. Striccoli, M. Curri, G.M. Liuzzi, N. Depalo, Luminescent PLGA nanoparticles for delivery of darunavir to the brain and inhibition of matrix metalloproteinase-9, a relevant therapeutic target of HIV-associated neurological disorders, ACS Chem. Neurosci. 2 (22) (2011) 4286–4301, 8.
[39] A. Kefayat, S. Vaezifar, Biodegradable PLGA implants containing doxorubicin-loaded chitosan nanoparticles for treatment of breast tumor-bearing mice, Int. J. Biol. Macromol. 136 (2019) 48–56.
[40] D. Ding, Q. Zhu, Recent advances of PLGA micro/nanoparticles for the delivery of biomacromolecular therapeutics, Mater. Sci. Eng. C. Mater. Biol. Appl. 92 (2018) 1041–1060.
[41] G.Y. Wang, S.L. Rayner, R. Chung, B.Y. Shi, X.J. Liang, Advances in nanotechnology-based strategies for the treatments of amyotrophic lateral sclerosis, Mater. Today Bio 6 (2020) 100055.
[42] Y. Zhang, X. Wang, H. Yang, H. Liu, Y. Lu, L. Han, G. Liu, Kinase AKT controls innate immune cell development and function, Immunology 140 (2) (2013) 143–152.
[43] G. Muto, H. Kotani, T. Kondo, R. Morita, S. Tsuruta, T. Kobayashi, H. Luche, H. J. Fehling, M. Walsh, Y. Choi, A. Yoshimura, TRAF6 is essential for maintenance of regulatory T cells that suppress Th2 type autoimmunity, PLoS One 8 (9) (2013) e74639.
[44] K.S. Walker, M. Deak, A. Paterson, K. Hudson, P. Cohen, D.R. Alessi, Activation of protein kinase B beta and gamma isoforms by insulin in vivo and by 3-phosphoinositide-dependent protein kinase-1 in vitro: comparison with protein kinase B alpha (Pt 1), Biochem J. 331 (Pt 1) (1998) 299–308.
[45] B.E. Cristiano, J.C. Chan, K.M. Hannan, N.A. Lundie, N.J. Marmy-Conus, I. G. Campbell, W.A. Phillips, M. Robbie, R.D. Hannan, R.B. Pearson, A specific role for AKT3 in the genesis of ovarian cancer through modulation of G(2)-M phase transition, Cancer Res. 66 (24) (2006) 11718–11725.
[46] W. Wei, H.B. He, W.Y. Zhang, H.X. Zhang, J.B. Bai, H.Z. Liu, J.H. Cao, K.C. Chang, X.Y. Li, S.H. Zhao, miR-29 targets Akt3 to reduce proliferation and facilitate differentiation of myoblasts in skeletal muscle development, Cell Death Dis. 4 (6) (2013) e668.
[47] C.M. Anderson, J. Hu, R.M. Barnes, A.B. Heidt, I. Cornelissen, B.L. Black, Myocyte enhancer factor 2C function in skeletal muscle is required for normal growth and glucose metabolism in mice, Skelet. Muscle 5 (2015) 7.
[48] X. Chen, B. Gao, M. Ponnusamy, Z. Lin, J. Liu, MEF2 signaling and human diseases, Oncotarget 8 (67) (2017) 112152–112165.
[49] Z. Jiang, W. Wang, G. Perry, X. Zhu, X. Wang, Mitochondrial dynamic abnormalities in amyotrophic lateral sclerosis, Transl. Neurodegener. 4 (2015) 14.
[50] L.J. Martin, The mitochondrial permeability transition pore: a molecular target for amyotrophic lateral sclerosis therapy, Biochim. Biophys. Acta 1802 (1) (2010) 186–197.
[51] E.F. Smith, P.J. Shaw, K.J. De, Vos, The role of mitochondria in amyotrophic lateral sclerosis, Neurosci. Lett. 710 (2019) 132933.
[52] A. Echaniz-Laguna, J. Zoll, E. Ponsot, B. N'guessan, C. Tranchant, J.P. Loeffler, E. Lampert, Muscular mitochondrial function in amyotrophic lateral sclerosis is progressively altered as the disease develops: a temporal study in man, Exp. Neurol. 198 (1) (2006) 25–30.
[53] L. Dupuis, J.L. Gonzalez de Aguilar, H. Oudart, M. de Tapia, L. Barbeito, J. P. Loeffler, Mitochondria in amyotrophic lateral sclerosis: a trigger and a target, Neurodegener. Dis. 1 (6) (2004) 245–254.
[54] X. Xie, R. Shu, C. Yu, Z. Fu, Z. Li, Mammalian AKT, the emerging roles on mitochondrial function in diseases, Aging Dis. 13 (1) (2022) 157–174.
[55] D. Lian, M.M. Chen, H. Wu, S. Deng, X. Hu, The role of oxidative stress in skeletal muscle myogenesis and muscle disease, Antioxid. (Basel) 11 (4) (2022).
[56] M. Nagase, Y. Yamamoto, Y. Miyazaki, H. Yoshino, Increased oxidative stress in patients with amyotrophic lateral sclerosis and the effect of edaravone administration, Redox Rep. 21 (3) (2016) 104–112.
[57] D. Capitanio, M. Vasso, A. Ratti, G. Grignaschi, M. Volta, M. Moriggi, C. Daleno, C. Bendotti, V. Silani, C. Gelfi, Molecular signatures of amyotrophic lateral sclerosis disease progression in hind and forelimb muscles of an SOD1(G93A) mouse model, Antioxid. Redox Signal 17 (10) (2012) 1333–1350.
[58] E.M.C. Fisher, L. Greensmith, A. Malaspina, P. Fratta, M.G. Hanna, G. Schiavo, A. M. Isaacs, R.W. Orrell, T.J. Cunningham, A.A. Arozena, Opinion: more mouse models and more translation needed for ALS, Mol. Neurodegener. 18 (1) (2023) 30.